Small-kernel superresolution methods for microscanning imaging systems

Jiazheng Shi, Stephen E. Reichenbach, and James D. Howe

Two computationally efficient methods for superresolution reconstruction and restoration of microscanning imaging systems are presented. Microscanning creates multiple low-resolution images with slightly different sample–scene phase shifts. The digital processing methods developed here combine the low-resolution images to produce an image with higher pixel resolution (i.e., superresolution) and higher fidelity. The methods implement reconstruction to increase resolution and restoration to improve fidelity in one-pass convolution with a small kernel. One method uses a small-kernel Wiener filter and the other method uses a parametric cubic convolution filter. Both methods are based on an end-to-end, continuous–discrete–continuous microscanning imaging system model. Because the filters are constrained to small spatial kernels they can be efficiently applied by convolution and are amenable to adaptive processing and to parallel processing. Experimental results with simulated imaging and with real microscanned images indicate that the small-kernel methods efficiently and effectively increase resolution and fidelity.

OCIS codes: 100.6640, 100.3020, 100.2000.

1. Introduction

Improvements in the resolution and fidelity of digital imaging systems have substantial value for remote sensing, military surveillance, and other applications, especially those for which a large field of view is desirable and the distance to objects of interest cannot be reduced. Advances in optics and sensor technologies offer one path for increasing the spatial resolution and fidelity of imaging systems, but such hardware improvements can be costly or limited by physical constraints or both.[1,2] Digital image processing offers an alternative path for improving image quality.

Digital superresolution reconstruction and restoration methods can substantially increase resolution and fidelity of an imaging system. Reconstruction methods increase pixel resolution beyond that of the physical imaging system by estimating values on a finer grid or lattice. Restoration methods increase fidelity beyond that of the physical imaging system by correcting for acquisition artifacts such as blurring, aliasing, and noise. Superresolution reconstruction and restoration can be combined to produce images with greater resolution and higher fidelity.[3]

Typically, superresolution methods produce an enhanced image from multiple low-resolution images with either different sample–scene phase or with different blurring functions.[4,5] Microscanning is a systematic approach to acquiring images with slightly different sample–scene phases; between successive images the system is shifted slightly, either in a predetermined pattern or in a random pattern. As in most superresolution methods, the methods developed in this paper presume global sample–scene phase shifts.

Most superresolution methods can be decomposed into three tasks: registration, reconstruction, and restoration. These tasks can be implemented as separate steps or in one or two combined steps:

Registration is the process of orienting several images of a common scene with reference to a single coordinate system. Registering images to subpixel accuracy is a crucial factor that greatly affects superresolution processing. It may be trivial to register systems with precisely controlled phase shifting. Popular methods for subpixel image registration include phase or cross-correlation registration[6,7] and gradient-based registration.[8,9]

J. Shi (jshi@cse.unl.edu) and S. E. Reichenbach are with the Department of Computer Science and Engineering, University of Nebraska, Lincoln, Nebraska 68588-0115. J. D. Howe is with the Night Vision and Electronic Sensors Directorate, U.S. Army, Fort Belvoir, Virginia 22060.

Received 10 June 2005; revised 24 August 2005; accepted 25 August 2005.

0003-6935/06/061203-12$15.00/0

Report Documentation Page

Form Approved
OMB No. 0704-0188

1. REPORT DATE	2. REPORT TYPE	3. DATES COVERED
AUG 2005		**00-00-2005 to 00-00-2005**

4. TITLE AND SUBTITLE	5a. CONTRACT NUMBER
Small-kernel superresolution methods for microscanning imaging systems	5b. GRANT NUMBER
	5c. PROGRAM ELEMENT NUMBER
6. AUTHOR(S)	5d. PROJECT NUMBER
	5e. TASK NUMBER
	5f. WORK UNIT NUMBER
7. PERFORMING ORGANIZATION NAME(S) AND ADDRESS(ES) **Army Night Vision and Electronic Sensors Directorate,Fort Belvoir,VA,22060**	8. PERFORMING ORGANIZATION REPORT NUMBER
9. SPONSORING/MONITORING AGENCY NAME(S) AND ADDRESS(ES)	10. SPONSOR/MONITOR'S ACRONYM(S)
	11. SPONSOR/MONITOR'S REPORT NUMBER(S)

12. DISTRIBUTION/AVAILABILITY STATEMENT
Approved for public release; distribution unlimited

13. SUPPLEMENTARY NOTES

14. ABSTRACT

15. SUBJECT TERMS

16. SECURITY CLASSIFICATION OF:			17. LIMITATION OF ABSTRACT	18. NUMBER OF PAGES	19a. NAME OF RESPONSIBLE PERSON
a. REPORT **unclassified**	b. ABSTRACT **unclassified**	c. THIS PAGE **unclassified**	**Same as Report (SAR)**	**12**	

Image reconstruction is the process of estimating image value at arbitrary locations on a spatial continuum from a set of discrete samples. For superresolution imaging, the aim of reconstruction is to produce an image with pixels on a high-resolution grid with uniform spacing from multiple registered images, which may have pixels that are irregularly distributed. Popular methods for reconstruction include nearest-neighbor interpolation, bilinear interpolation, cubic-spline interpolation, piecewise cubic convolution, and cubic optimal maximal-order–minimal-support (o-Moms) interpolation.[10] Kriging, which originated in the geostatistic community, is a popular method for interpolating spatial data.[11,12]

Image restoration is the process of recovering a more accurate image of a scene by correcting or reducing degradations such as acquisition blurring, aliasing, and noise.[13] Basic methods for image restoration include deconvolution, use of least-squares filters, and iterative approaches.[14]

Digital processing for superresolution is an area of active research.[1,15] Approaches based on nonuniform interpolation are the most intuitive. Computational efficiency is their major advantage. For example, Alam *et al.* proposed a superresolution method for infrared images, in which a gradient-based method to estimate shift, a weighted nearest-neighbor approach to align irregularly displaced low-resolution images to form a superresolution image, and finally a Wiener filter for image restoration are used.[9] However, nonuniform interpolation approaches do not account for variations in acquisition conditions for the low-resolution images or guarantee the optimality of the end-to-end imaging system.[3] Tsai and Huang investigated superresolution imaging in the frequency domain,[16] using the shift theorem of the Fourier transform and the aliasing relationship between low-resolution images and the ideal superresolution image. High-frequency components are extracted from aliased low-frequency components. Kim *et al.* extended this approach for blurred and noisy images and developed a weighted recursive least-squares algorithm.[17,18] Unfortunately, Fourier-domain methods are computationally costly. Superresolution methods based on stochastic theories employ *a priori* knowledge about a scene and noise. For example, Shultz and Stevenson[19] proposed a Bayesian restoration with a discontinuity-preserving prior-image model, and Elad and Feuer[5] and Elad and Hel-Or[20] approached superresolution by unifying the maximum-likelihood, maximum *a posteriori*, and projection onto convex set. Stochastic approaches also may have high computational complexity and suboptimality for an end-to-end imaging system. Computationally efficient spatial-domain methods have been proposed. Nguyen and Milanfar[21] proposed efficient block circulant preconditioners for solving the Tikhonov regularized superresolution problems by using the conjugate gradient method, but the method requires perfect shift estimation.[22] Farsiu *et al.* proposed a robust method that defines the cost function of regularization by use of the L_1 norm minimization.[23] The method is robust for estimation errors of shift and noise, but the system model accounts only for acquisition in the end-to-end system, and the proposed fast solution is iterative. Even though interpolation and restoration are done simultaneously, computational costs for real-time applications are a concern with iterative methods.

In this paper we investigate superresolution methods for microscanning imaging systems that can be implemented efficiently with small convolution kernels. The approach is based on an end-to-end continuous–discrete–continuous (CDC) system model that accounts for the fundamental trade-off in imaging system design between acquisition blurring related to optics, detectors, and analog circuits and aliasing owing to sampling. The system model also accounts for noise associated with unpredictable signal and system variations and quantization, for misregistration of the low-resolution images, and for the display system. The approach uses one-pass convolution with small kernels for computationally efficient reconstruction and restoration. This approach also is amenable to adaptive processing and to parallel processing with appropriate hardware support.

The rest of this paper is organized as follows: in Section 2 we present the CDC system model, introduce microscanning, and formulate the system's fidelity. In Section 3 we derive superresolution reconstruction and restoration filters, including the optimal Wiener filter, a spatially constrained Wiener kernel, and a parametric cubic convolution kernel. In Section 4 we present experimental results for images from a simulation and from a real imaging system. In Section 5 we summarize this paper and describe issues for future work.

2. System Model and Problem Formulation

In this section we present the CDC system model, describe microscanning, and formulate the fidelity of a microscanning imaging system based on the system model. The system model is introduced in the spatial domain of the image, but the problem and fidelity analysis are formulated in the Fourier frequency domain, so spatial convolution can be considered pointwise multiplication of transform coefficients.

A. Continuous–Discrete–Continuous System Model

The superresolution methods developed in this paper are based on the CDC model pictured in Fig. 1. This imaging system model is relatively simple, yet it captures the most significant degradations in typical imaging systems: linear shift-invariant blurring characterized by acquisition point-spread function (PSF) h; aliasing, which is due to sampling a continuous function on a uniform, rectangular lattice $\perp\!\!\!\perp\!\!\!\perp$; additive system noise e; and display, characterized by display PSF d.

With this model, a single low-resolution digital image p is defined mathematically as

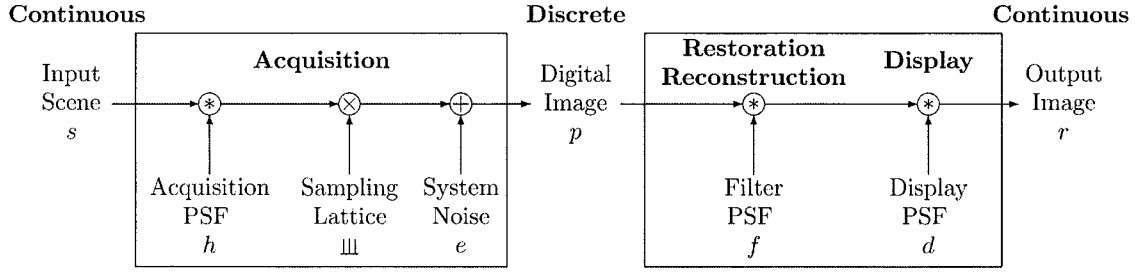

Fig. 1. End-to-end model of the digital imaging process.

$$p[m,\ n] = \int\int s(x,\ y)h(m-x,\ n-y)\mathrm{d}x\mathrm{d}y + e[m,\ n], \tag{1}$$

where $[m, n]$ are integer pixel indices for digital image p and (x, y) are continuous coordinates for scene s. For notational convenience, and without loss of generality, the spatial coordinates are normalized in units of the sampling interval. In practice, the spatial extent of the image is finite, but that issue is not significant for the following analyses.

Restoration and reconstruction can be implemented in one step by convolution of image p with filter PSF f to produce a processed image of arbitrary resolution, which can then be displayed. Modeling the display as a linear shift-invariant process characterized by display PSF d yields continuous output image r:

$$r(x,\ y) = \int\int \Big[\sum_m \sum_n p[m,\ n]f(x'-m,\ y'-n)\Big] \times d(x-x',\ y-y')\mathrm{d}x'\mathrm{d}y'. \tag{2}$$

B. Microscanning

Microscanning is the process of generating multiple images from a common scene by shifting either the scene or the image-acquisition system. The shifting can be performed in a regular pattern or an irregular pattern. Figure 2 illustrates the microscanning process for a sequence of images p_k, $k = 0 \ldots K-1$, with an unchanging scene shifted between images, variable blur and noise, and a fixed sampling grid. (Reverse shifting of the sampling grid for a fixed scene produces the same images.) Then microscanned image p_k is

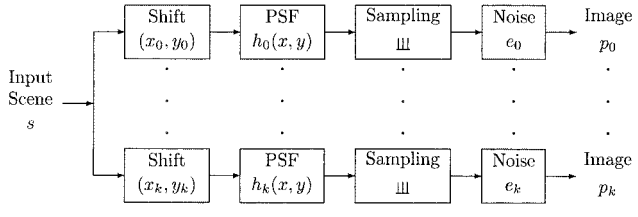

Fig. 2. Microscanning produces multiple images.

$$p_k[m,\ n] = \int\int s(x-x_k,\ y-y_k) \times h_k(m-x,\ n-y)\mathrm{d}x\mathrm{d}y + e_k[m,\ n], \tag{3}$$

where k is the index for the microscanning image, (x_k, y_k) is the relative shift, h_k is the acquisition PSF, and e_k is the additive system noise.

Image acquisition (with blurring, sampling, and noise), digital processing (for registration, reconstruction, and restoration), and display of microscanned imaging are analyzed more easily in the Fourier frequency domain, regardless of whether digital image processing is performed in the spatial domain or in the frequency domain. In the frequency domain, the Fourier transform of microscanned image p_k [the transform of Eq. (3)] is

$$\hat{p}_k(u,\ v) = \sum_\mu \sum_\nu \hat{s}(u-\mu,\ v-\nu)\hat{h}_k(u-\mu,\ v-\nu) \times \exp\{-i2\pi[(u-\mu)x_k + (v-\nu)y_k]\} + \hat{e}_k(u,\ v), \tag{4}$$

where a circumflex indicates a Fourier transform. In Eq. (4) the frequency-domain equivalent for spatial-domain blurring by convolution in Eq. (3) is pointwise multiplication of the transform coefficients of the scene and the PSF. The frequency-domain equivalent for spatial-domain sampling is the double sum, which folds the transform coefficients.

The microscanned images must be registered relative to one another. In the frequency domain the registered and combined microscanned images are

$$\begin{aligned}\hat{p}(u,\ v) &= \frac{1}{K}\sum_{k=0}^{K-1}\hat{p}_k(u,\ v)\exp\{i2\pi[u(x_k + \alpha_k) + v(y_k + \beta_k)]\} \\ &= \frac{1}{K}\sum_\mu\sum_\nu \hat{s}(u-\mu,\ v-\nu) \times \sum_{k=0}^{K-1}\hat{h}_k(u-\mu,\ v-\nu)\exp[i2\pi(u\alpha_k + v\beta_k)] \\ &\quad \times \exp[i2\pi(\mu x_k + \nu y_k)] + \frac{1}{K}\sum_{k=0}^{K-1} e_k(u,\ v)\exp\{i2\pi[u(x_k+\alpha_k) + v(y_k+\beta_k)]\},\end{aligned} \tag{5}$$

where (α_k, β_k) is the registration error for image p_k. Mathematically, the registered images are combined by addition. If registration is perfect, then $\alpha_k = \beta_k = 0$, and each microscanned image is shifted to its proper position in the registered image.

In the Fourier frequency domain, reconstruction and restoration of the scene are products of the Fourier transform of registered image $\hat{p}$ and filter transfer function $\hat{f}$. Then the display process multiplies that result by display transfer function $\hat{d}$:

$$\hat{r}(u, v) = \hat{p}(u, v)\hat{f}(u, v)\hat{d}(u, v). \quad (6)$$

C. Fidelity Analysis

By Rayleigh's theorem, the expected mean square error (MSE) of the CDC imaging system for an ensemble of scenes can be analyzed in either the spatial or the frequency domain:

$$\epsilon^2 = \varepsilon\left\{\int\int |r(x, y) - s(x, y)|^2 \, dxdy\right\} = \varepsilon\left\{\int\int |\hat{r}(u, v) - \hat{s}(u, v)|^2 \, dudv\right\}. \quad (7)$$

In the following analysis it is assumed that the power spectra of the scene ensemble and the noise are known, that the scene and the noise are uncorrelated, that coaliased components of the sampled scene are uncorrelated, and that the noise between images is uncorrelated[24]:

$$\varepsilon[\hat{s}(u, v)\hat{s}^*(u - \mu, v - \nu)] = \begin{cases} \hat{\Phi}_s(u, v) & (\mu, \nu) = (0, 0) \\ 0 & \text{otherwise} \end{cases},$$

$$\varepsilon[\hat{e}_j(u, v)\hat{e}_k^*(u, v)] = \begin{cases} \hat{\Phi}_{e_k}(u, v) & j = k \\ 0 & \text{otherwise} \end{cases},$$

$$\varepsilon[\hat{s}(u - \mu, v - \nu)\hat{e}_k^*(u, v)] = 0, \quad (8)$$

where the asterisk denotes complex conjugation, $\hat{\Phi}_s$ is the power spectrum of the scene, and $\hat{\Phi}_{e_k}$ is the power spectrum of the noise. For convenience, and without loss of generality, scenes are normalized such that the mean and the variance are 0 and 1, respectively.

The expected MSE ϵ^2 for the CDC imaging system can be expressed in terms of the scene and noise power spectra, the acquisition transfer function, the relative shifts and registration errors, the reconstruction and restoration filter, and the display transfer function:

$$\epsilon^2 = \int\int \big[\hat{\Phi}_s(u, v) - \hat{f}(u, v)\hat{d}(u, v)\hat{\Phi}_{s,p}^*(u, v) - \hat{f}^*(u, v)\hat{d}^*(u, v)\hat{\Phi}_{s,p}(u, v) + |\hat{f}(u, v)|^2 |\hat{d}(u, v)|^2 \hat{\Phi}_p(u, v)\big] du dv, \quad (9)$$

where $\hat{\Phi}_p$ is the power spectrum of the registered image and $\hat{\Phi}_{s,p}$ is the cross-power spectrum of the scene and the registered image:

$$\begin{aligned}
\hat{\Phi}_p(u, v) &= \varepsilon\,[|\hat{p}(u, v)|^2] \\
&= \frac{1}{K^2}\sum_\mu\sum_\nu \hat{\Phi}_s(u - \mu, v - \nu) \\
&\quad \times \left|\sum_{k=0}^{K-1} \hat{h}_k(u - \mu, v - \nu)\varepsilon\{\exp[i2\pi \times (u\alpha_k + v\beta_k)]\exp[i2\pi \times (\mu x_k + \nu y_k)]\}\right|^2 + \frac{1}{K^2}\sum_{k=0}^{K-1} \hat{\Phi}_{e_k}(u, v), \\
\hat{\Phi}_{s,p}(u, v) &= \varepsilon[\hat{s}(u, v)\hat{p}^*(u, v)] \\
&= \hat{\Phi}_s(u, v)\frac{1}{K}\sum_{k=0}^{K-1} \hat{h}_k^*(u, v)\varepsilon\{\exp[-i2\pi \times (u\alpha_k + v\beta_k)]\}.
\end{aligned} \quad (10)$$

If the distribution of the registration errors is known, the expressions for the expected MSEs can be analyzed with respect to those errors. For example, if α_k and β_k are uniformly distributed in the intervals

$$\left[-\frac{1}{2W_x}, \frac{1}{2W_x}\right], \quad \left[-\frac{1}{2W_y}, \frac{1}{2W_y}\right],$$

respectively, then, because

$$\int_{-\frac{1}{2W_x}}^{\frac{1}{2W_x}}\int_{-\frac{1}{2W_y}}^{\frac{1}{2W_y}} \exp[i2\pi(u\alpha_k + v\beta_k)]W_xW_y d\alpha_k d\beta_k = \mathrm{sinc}(u/W_x)\mathrm{sinc}(v/W_y), \quad (11)$$

the components of the expected MSEs are

$$\begin{aligned}
\hat{\Phi}_p(u, v) &= \frac{1}{K^2}\,\mathrm{sinc}^2(u/W_x)\mathrm{sinc}^2(v/W_y) \\
&\quad \times \sum_\mu\sum_\nu \hat{\Phi}_s(u - \mu, v - \nu) \\
&\quad \times \left|\sum_{k=0}^{K-1} \hat{h}_k(u - \mu, v - \nu)\exp[i2\pi(\mu x_k + \nu y_k)]\right|^2 + \frac{1}{K^2}\sum_{k=0}^{K-1} \hat{\Phi}_{e_k}(u, v), \\
\hat{\Phi}_{s,p}(u, v) &= \mathrm{sinc}(u/W_x)\mathrm{sinc}(v/W_y) \\
&\quad \times \hat{\Phi}_s(u, v)\frac{1}{K}\sum_{k=0}^{K-1} \hat{h}_k^*(u, v).
\end{aligned} \quad (12)$$

$\hat{\Phi}_p$ is subject to relative shifts (x_k, y_k). For instance, if

the number of microscanned images K is 2, $\hat{\Phi}_p$ for relative shifts $\{(x_0, y_0) = (0, 0),\ (x_1, y_1) = (0, 0.5)\}$ is the same as for relative shifts $\{(x_0, y_0) = (0.5, 0), (x_1, y_1) = (0.5, 0.5)\}$ but is different from that for relative shifts $\{(x_0, y_0) = (0, 0), (x_1, y_1) = (0.5, 0)\}$ and for $\{(x_0, y_0) = (0, 0.5), (x_1, y_1) = (0.5, 0.5)\}$. Filters derived with respect to $\hat{\Phi}_p$ can vary, depending on the relative shift pattern of microscanned images.

Fidelity[25] is a normalized measure of image quality based on the MSE:

$$\mathcal{F} = 1 - \frac{\epsilon^2}{\int\int \hat{\Phi}_s(u, v)\mathrm{d}u\mathrm{d}v}. \tag{13}$$

The greatest fidelity possible is 1 when the MSE is 0. In Section 3 we derive superresolution reconstruction and restoration filters that maximize fidelity $\mathcal{F}$ (or equivalently minimize the MSE, ϵ^2).

3. Superresolution Reconstruction and Restoration

The techniques developed in this section are designed for performance of reconstruction and restoration. The methods take as input multiple images that have been registered and produce a single output image with high fidelity and superresolution.

A. CDC Wiener Filter

For comparison of performance, it is useful to derive the optimal CDC Wiener filter.[24] Denoting MSE as a functional of the filter transfer function $\hat{f}(u, v)$ yields

$$\epsilon^2(\hat{f}) = \int\int L(u, v, \hat{f})\mathrm{d}u\mathrm{d}v, \tag{14}$$

where

$$\begin{aligned} L(u, v, \hat{f}) = {} & \hat{\Phi}_s(u, v) - \hat{f}(u, v)\hat{d}(u, v)\hat{\Phi}_{s,p}(u, v) \\ & - \hat{f}^*(u, v)\hat{d}^*(u, v)\hat{\Phi}_{s,p}{}^*(u, v) \\ & + \left|\hat{f}(u, v)\right|^2\left|\hat{d}(u, v)\right|^2 \hat{\Phi}_p(u, v). \end{aligned} \tag{15}$$

The optimal filter must satisfy

$$\begin{aligned} \frac{\partial L}{\partial \hat{f}} &= \hat{f}^*(u, v)\left|\hat{d}(u, v)\right|^2\hat{\Phi}_p(u, v) - \hat{d}(u, v)\hat{\Phi}_{s,p}{}^*(u, v) \\ &= 0, \end{aligned} \tag{16}$$

so the optimal filter is

$$\hat{f}_w(u, v) = \frac{\hat{\Phi}_{s,p}(u, v)}{\hat{\Phi}_p(u, v)}\frac{\hat{d}^*(u, v)}{\left|\hat{d}(u, v)\right|^2} = \frac{\hat{\Phi}_{s,\bar{p}}(u, v)}{\hat{\Phi}_{\bar{p}}(u, v)}, \tag{17}$$

where $\hat{\Phi}_{\bar{p}}$ and $\hat{\Phi}_{s,\bar{p}}$ are introduced to incorporate the effects of the display device on the image (and are used in the derivations of the small kernels in the following sections). The CDC Wiener filter cannot be implemented practically by means of spatial convolution because it is continuous and its support is the full extent of the image. As described in Subsection 3.B, one can reduce the computational costs of superresolution reconstruction and restoration by constraining the spatial support of the filter to a small kernel.

B. Small-Kernel Wiener Filter

The derivation of small-kernel Wiener filter f_c is conditioned on constraints imposed on its spatial support. The support of the kernel is a nonempty set of spatial discrete locations C for which filter values can be nonzero. Except for locations in the support set, the filter value is 0:

$$f_c(x, y) = 0, \quad (x, y) \notin C. \tag{18}$$

The larger the filter support, the better the performance, but small kernels can be highly effective.[26]

We derive the optimal, spatially constrained filter by minimizing MSE ϵ^2 with respect to the elements in C, which mathematically requires that

$$\frac{\partial \epsilon^2}{\partial f_c(x, y)} = 0, \quad \forall (x, y) \in C. \tag{19}$$

These constraints can be expressed in a system of linear equations[26]:

$$\sum_{(x', y') \in C} \Phi_{\bar{p}}(x - x', y - y')f_c(x', y') = \Phi_{s,\bar{p}}(x, y), \quad \forall (x, y) \in C, \tag{20}$$

where $\hat{\Phi}_{\bar{p}}$ is the autocorrelation of the displayed image and $\hat{\Phi}_{s,\bar{p}}$ is the cross correlation of the scene and the displayed image. The number of equations and the number of unknowns are both equal to the number of elements in support set C; i.e., there are $|C|$ equations in $|C|$ unknowns.

C. Parametric Cubic Convolution

Piecewise cubic convolution is a popular interpolation method for image reconstruction that is traditionally implemented by separable convolution with a small one-dimensional kernel consisting of piecewise cubic polynomials.[27,28] One can generalize this popular method to two dimensions and reformulate it by relaxing constraints to perform reconstruction and restoration in one pass with small-kernel convolution.[29] With constraints for symmetry, continuity, and smoothness, the two-dimensional kernel with support $[-2, 2] \times [-2, 2]$ has five parameters $\{a_1, a_2, a_3, a_4, a_5\}$:

$$\begin{aligned} f_p(x, y) = {} & f_0(x, y) + a_1 f_1(x, y) + a_2 f_2(x, y) \\ & + a_3 f_3(x, y) + a_4 f_4(x, y) + a_5 f_5(x, y), \end{aligned} \tag{21}$$

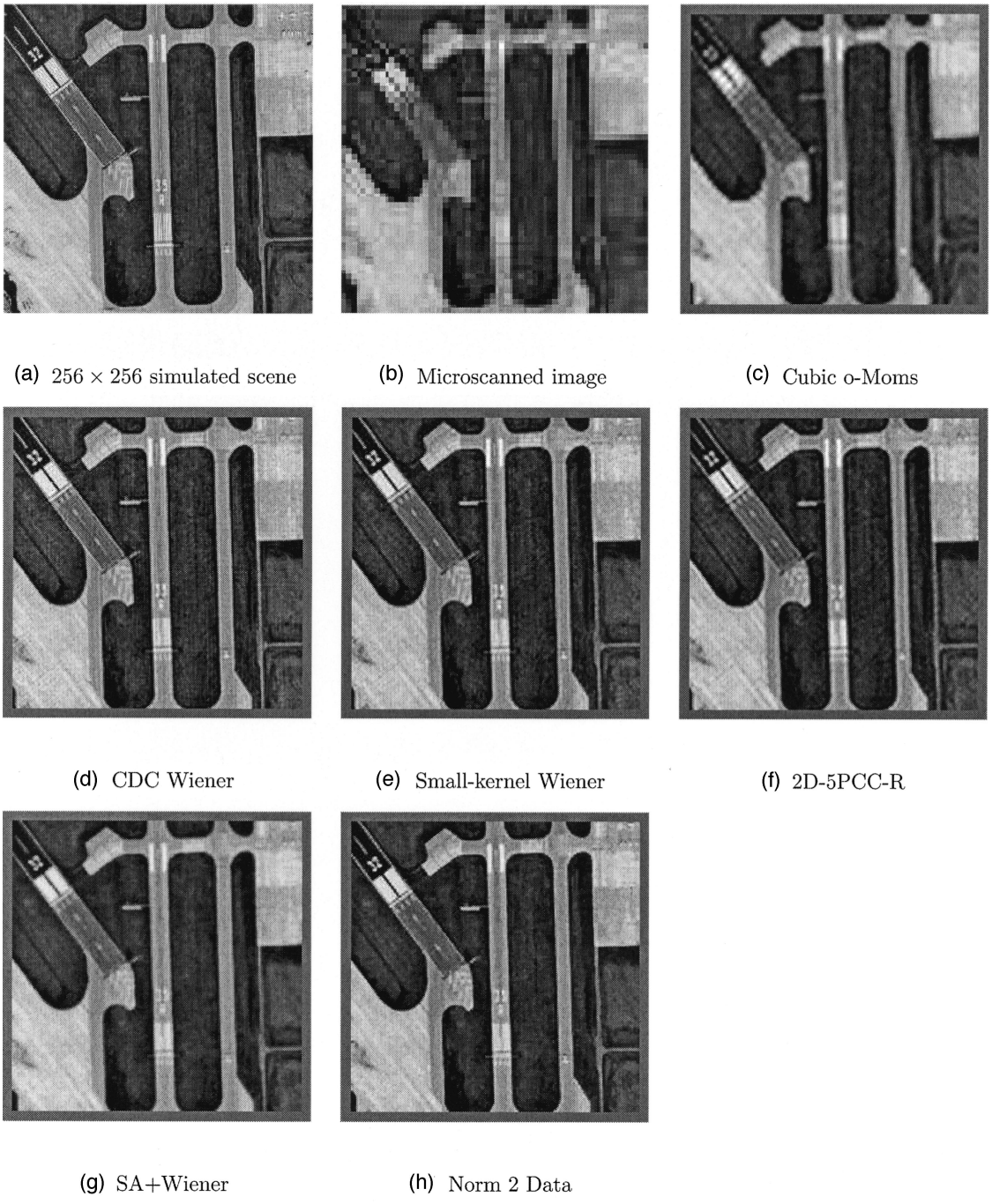

(a) 256 × 256 simulated scene (b) Microscanned image (c) Cubic o-Moms

(d) CDC Wiener (e) Small-kernel Wiener (f) 2D-5PCC-R

(g) SA+Wiener (h) Norm 2 Data

Fig. 3. Simulation results.

where f_0–f_5 are defined in Appendix A. This kernel, designated 2D-5PCC-R (to distinguish it from two-dimensional piecewise cubic interpolation[30]), is a continuous function.

One can derive the optimal 2D-5PCC-R kernel f_p for an ensemble of scenes by minimizing the MSE ϵ^2 with respect to the five parameters. Computing the partial derivatives of ϵ^2 with respect to the parameters and solving for simultaneous equality with zero:

$$\frac{\partial \epsilon^2}{\partial a_1} = \frac{\partial \epsilon^2}{\partial a_2} = \frac{\partial \epsilon^2}{\partial a_3} = \frac{\partial \epsilon^2}{\partial a_4} = \frac{\partial \epsilon^2}{\partial a_5} = 0, \tag{22}$$

yields five equations for the optimal parameter value:

$$\int\int \hat{f}_i(u, v)\left\{\mathrm{Re}\left[\hat{\Phi}_{s,\bar{p}}(u, v)\right] - \hat{f}_0(u, v)\hat{\Phi}_{\bar{p}}(u, v)\right\}\mathrm{d}u\mathrm{d}v = \int\int \hat{f}_i(u, v)\left[\hat{f}_p(u, v) - \hat{f}_0(u, v)\right]\hat{\Phi}_{\bar{p}}(u, v)\mathrm{d}u\mathrm{d}v,$$

$$i = 1 \ldots 5. \tag{23}$$

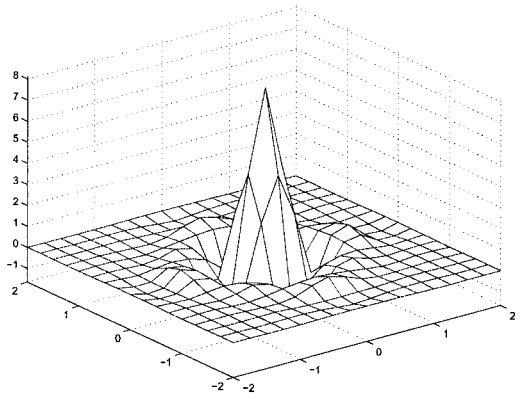

(a) Small-kernel Wiener filter

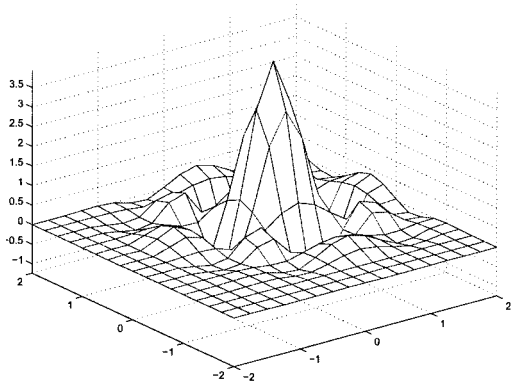

(b) 2D-5PCC-R

Fig. 4. Small reconstruction and restoration kernels for the simulation experiment.

4. Experimental Results

In this section we present experimental results for a simulated imaging system and for real images. In the simulation the scene is a high-resolution digital image. The simulated scene is blurred, sampled, and degraded by noise (by digital processing) to produce simulated microscanned images. These images are reconstructed and restored by the optimal CDC Wiener filter, by the small-kernel Wiener filter, by the 2D-5PCC-R filter, by shift-and-add with Wiener deconvolution, denoted SA + Wiener,[20,31] and by norm 2 data with L_1 regularization (denoted Norm 2 Data).[23,31]

We implement the superresolution computations for the optimal Wiener filter in the Fourier frequency domain by multiplying the filter defined in Eq. (17) by the Fourier transform of the registered, combined images defined in Eq. (5). The computations for the small-kernel Wiener filter and the 2D-5PCC-R filter are implemented in the spatial domain, for computational efficiency, by convolution of the registered combined images with the small kernels defined by the solutions for Eqs. (20) and (23), respectively. Both SA + Wiener and Norm 2 Data were developed at the multidimensional Signal Processing Research Group at the University of California, Santa Cruz.[31] Norm 2 Data is an iterative superresolution method, and these experiments use default parameter values (except the deconvolution kernel) of the software.

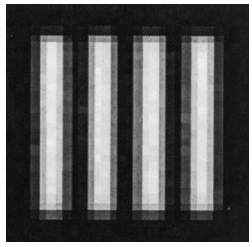

Fig. 5. Low-resolution infrared image of a four-bar target used for estimating the acquisition transfer function.

For simulated imaging, all resultant images are compared to the original scene. Because the phase shifts between the simulated scene and the microscanned images are known, the simulation facilitates true quantitative measures of reconstruction and restoration performance. We also apply the superresolution methods to real images acquired by panning an infrared camera slowly across a fixed scene. Because the true scene values are unknown, quantitative evaluation is not possible. Also, the microscanning shifts must be estimated, so the results are affected by registration error. Nonetheless, real images are useful for qualitatively demonstrating the effectiveness of the small-kernel methods in practice.

A. Simulation Results

Figure 3(a) illustrates a 256 × 256 digital image acquired by aerial photography[32] that is used as a simulated scene, and it is therefore the ideal superresolution image. The simulated scene is blurred by a Gaussian low-pass filter to simulate acquisition blurring:

$$\hat{h}(u, v) = \exp\left[-\left(u^2 + v^2\right)\right], \tag{24}$$

so the system transfer function at the Nyquist limit along each axis is $\hat{h}(0.0, 0.5) = \hat{h}(0.5, 0.0) = 0.779$.

Table 1. Fidelity and Computational Costs of Various Methods

	Computation Method					
Performance Metric	CDC Wiener	Small-Kernel Wiener	2D-5PCC-R	o-Moms	SA + Wiener	Norm 2 Data
Fidelity	0.980	0.975	0.966	0.928	0.966	0.979
Preprocessing time (s)	0.521	0.781	0.940	0.000	0.150	0.000
Filtering time (s)	0.121	0.030	0.030	0.120	0.380	49.121

After blurring, sixteen 64×64 low-resolution images are created with simulated microscanning at quarter-pixel intervals along each axis. In each simulated microscanned image, Gaussian white noise is added to each pixel such that the blurred signal-to-noise ratio (BSNR) is 30 dB:

$$\mathrm{BSNR} = 10 \log 10\left(\sigma_p{}^2/\sigma_e{}^2\right), \tag{25}$$

where $\sigma_p{}^2$ is the variance of the blurred microscanned images (after blurring and before additive noise) and $\sigma_e{}^2$ is the variance of the noise. Figure 3(b) illustrates one of the microscanned images (reference image p_0) interpolated back to 256×256 resolution by nearest-neighbor interpolation to show the granularity of the sampling. Figure 3(c) illustrates a higher-quality interpolation obtained with cubic o-Moms.[33] Four of the sixteen microscanned images are used for deriving the reconstruction and restoration filters and for superresolution processing:

×	O	×	O
O	O	O	O
×	O	×	O
O	O	O	O

where × and O, respectively, stand for locations (at quarter-pixel intervals) with and without samples.

The actual scene power spectrum is used to derive the optimal CDC Wiener filter to benchmark the optimal fidelity. The power spectrum for optimizing the small-kernel Wiener filter and the 2D-5PCC-R filter, however, is estimated (as typically is required in practice) using the power-spectrum model of a two-dimensional isotropic Markov random field (MRF).[34] The model can be fitted to the image power spectrum[30] or interactively parameterized for visual quality (as is done here). The MRF autocorrelation is

$$\Phi_s(x, y) = \exp\left(-\sqrt{x^2 + y^2}/\rho\right), \tag{26}$$

where ρ is the mean spatial detail of the scene in pixel units. The mean spatial detail can be interpreted as the average size of the details in the scene. In terms of the Hankel transform,[35] the power spectrum of the isotropic MRF is

$$\hat{\Phi}_s(u, v) = \frac{2\pi\rho^2}{\left[1 + 4\pi^2\rho^2\left(u^2 + v^2\right)\right]^{3/2}}. \tag{27}$$

The CDC Wiener filter, the small-kernel Wiener filter with support limited to $[-2, 2] \times [-2, 2]$, and the 2D-5PCC-R filter were derived for this simulation based on the isotropic MRF scene model with a mean spatial detail of 4 pixels. Figure 5 illustrates the small-kernel Wiener PSF [Fig. 4(a)] and the 2D-5PCC-R PSF [Fig. 4(b)]. The optimal parameter values for 2D-5PCC-R are $a_1 = 74.176$, $a_2 = -95.360$, $a_3 = 16.804$, $a_4 = -0.967$, and $a_5 = 0.238$.

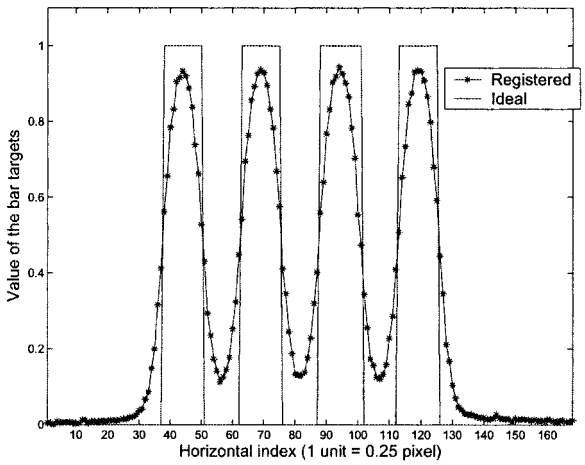

Fig. 6. Superresolution average scan of the bar target.

Figure 3(d)–3(h) presents the simulation results for the superresolution methods. To limit boundary effects, the borders of all resultant images are cleared. Visually, the superresolution images produced by all the restoration and reconstruction filters [Figs. 3(d)–3(h)] are better than provided by a single frame [Figs. 3(b) and 3(c)]. For example, the small, lightly colored rectangle in the upper-left quadrant between the diagonal runway and the leftmost vertical runway are clearer in the superresolution images. The images produced by the five superresolution methods are of similar visual quality, but the CDC Wiener filter appears to produce the best image and the SA + Wiener filter appears to produce the worst image. The image produced by the small-kernel Wiener filter appears to be slightly sharper than the image produced by the 2D-5PCC-R filter.

Table 1 lists the quantitative fidelity and computational costs for the various methods with the simulation. The computational costs were measured in seconds, averaged over multiple runs by MATLAB

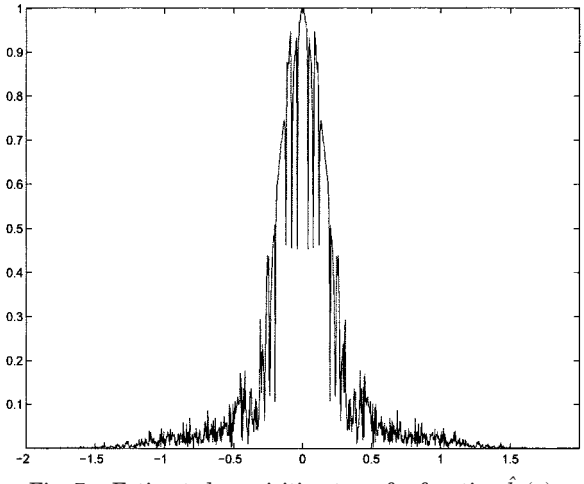
Fig. 7. Estimated acquisition transfer function $\hat{h}_x(u)$.

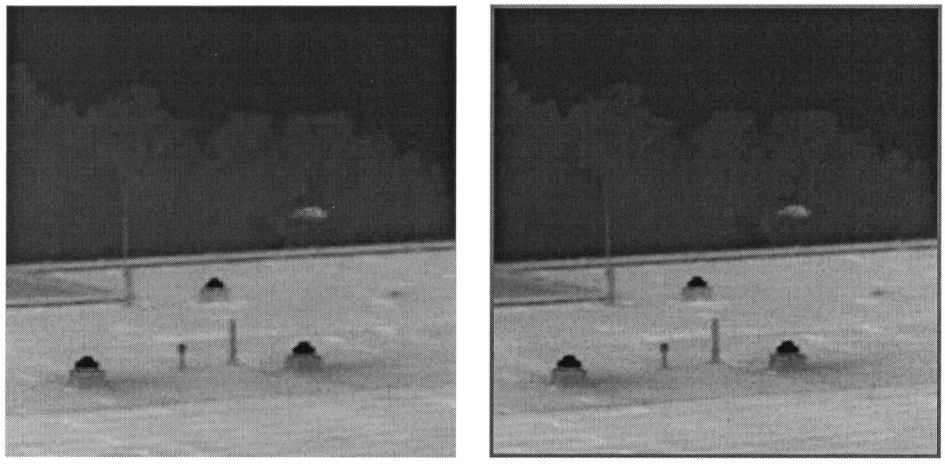

(a) 256 × 256 frame

(b) Cubic o-Moms

(c) Small-kernel Wiener filter

(d) 2D-5PCC-R

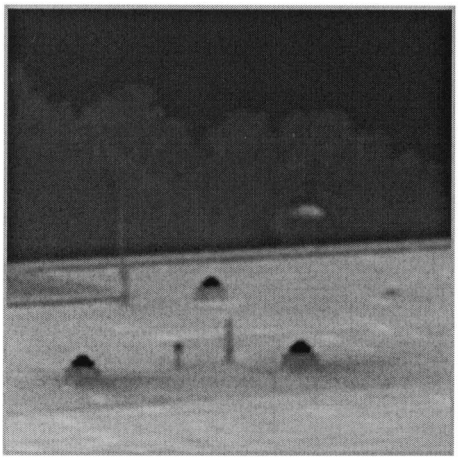

(e) SA+Wiener

(f) Norm 2 Data

Fig. 8. Superresolution results for a microscanned infrared system.

6.5 Release 13 program on an IBM R32 (Intel Pentium M 1.8 GHz CPU, 256 MB RAM, MS Windows XP Professional 2002). The optimal CDC Wiener filter (which uses the actual scene power spectrum) has the highest fidelity, as expected mathematically. The CDC Wiener filter requires preprocessing for computing the filter (which then can be used to filter multiple images) and requires forward and inverse Fourier transforms for application of the filter. As expected, the image from the cubic o-Moms with a single frame

has the lowest fidelity. The iterative method, Norm 2 Data, has a fidelity nearly equal to that of the CDC Wiener filter but requires 50 iterations and nearly 50 s for Fig. 3(h). Of the three small-kernel filters that can be efficiently applied by spatial convolution, the small-kernel Wiener filter has somewhat higher fidelity than the 2D-5PCC-R or the SA + Wiener filter.

The visual and quantitative results for the simulation indicate that the small-kernel Wiener filter and 2D-5PCC-R effectively improve image quality with efficient spatial-domain processing.

B. Results for Real Images

The superresolution reconstruction and restoration methods require characterizations of the system, including the noise power spectrum and acquisition transfer function. Noise can be characterized accurately from flat-field calibration images or from regions of uniform background of acquired images. The transfer function can be estimated to frequencies beyond the Nyquist limit by use of a knife-edge technique with images for various sample–scene phase shifts.[36] Microscanning provides such images.

For this experiment with real images, the acquisition transfer function of an infrared camera system was estimated from microscanned images of a four-bar target. The camera platform was microscanned as low-resolution images were recorded. Figure 5 illustrates a small piece of one of the 256 × 256 low-resolution images from the microscanned sequence. Employing the superresolution knife-edge technique,[36] we obtained and averaged a sequence of 120 low-resolution images of the bar target with subpixel accuracy (to 0.25 pixel). Figure 6 illustrates the resultant superresolution horizontal slice across the four-bar targets, superimposed upon the model of the bar target scene estimated by thresholding of the registered slice.

Figure 7 illustrates the modulation transfer function estimated by the CDC Wiener filter. For this experiment the two-dimensional acquisition transfer function was modeled as the separable product of the one-dimensional estimate:

$$\hat{h}(u, v) = \hat{h}_x(u)\hat{h}_x(v). \tag{28}$$

A more accurate estimate of the two-dimensional acquisition transfer function could be made from two or more slices.

In this experiment, the goal of superresolution reconstruction and restoration is to generate a 1024 × 1024, high-fidelity image from multiple microscanned 256 × 256 images. Figure 8(a) illustrates one of a microscanned sequence of low-resolution images from the infrared camera system, interpolated to 1024 × 1024 by nearest-neighbor interpolation. The scene is modeled as a modulation transfer function with a mean spatial detail equal to 8 pixels. The blurred signal-to-noise ratio was estimated to be 30 dB.

Figure 9 illustrates the small-kernel Wiener and cubic convolution reconstruction and restoration kernels, based on these system characterizations. The optimal parameter values for 2D-5PCC-R are $a_1 = -1.052$, $a_2 = -7.033$, $a_3 = 7.584$, $a_4 = -1.123$, and $a_5 = 0.137$. The small-kernel Wiener PSF provides more sharpening.

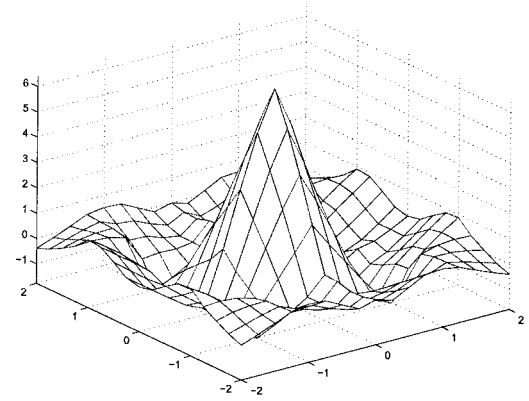

(a) Small-kernel Wiener filter

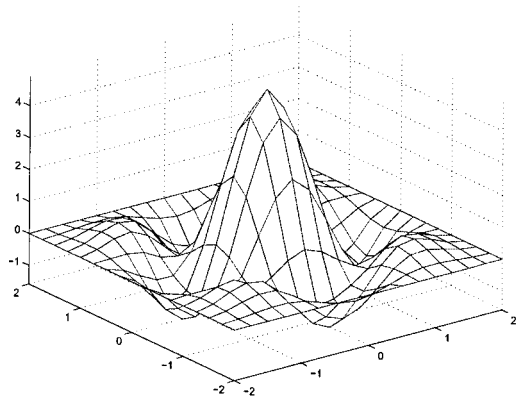

(b) 2D-5PCC-R

Fig. 9. Small reconstruction and restoration kernels for the real image experiment.

Figure 8(b) illustrates a 1024 × 1024 image reconstructed from a single image by cubic o-Moms. Figures 8(c)–8(f) illustrate 1024 × 1024 images reconstructed and restored with the small-kernel Wiener filter, 2D-5PCC-R, SA + Wiener, and Norm 2 Data. These results were generated from just three 256 × 256, microscanned low-resolution images with different relative shifts. The relative shift pattern for the three images is

×	×	O	×
O	O	O	O
O	O	O	O
O	O	O	O

To limit boundary effects, the borders of the processed images are cleared. Visually the resultant images in Figs. 8(c), 8(d), and 8(f) from superresolution reconstruction and restoration are substantially better than a single image in either Fig. 8(a) or Fig. 8(b).

Figure 9(e) from the SA + Wiener superresolution method is blurred. The superresolution image from the small-kernel Wiener filter is slightly sharper than the image from 2D-5PCC-R, consistent with the simulation results.

5. Conclusions

Images with superresolution and high fidelity are required in many imaging applications. In this paper we have investigated superresolution methods for microscanning imaging systems that efficiently implement reconstruction and restoration with small convolution kernels. The approach is based on an end-to-end system model that accounts for the fundamental trade-off in imaging system design between acquisition and aliasing. The system model also accounts for noise, misregistration of the low-resolution images, and the display system. Computationally efficient reconstruction and restoration are achieved by use of one-pass convolution with small kernels.

We have developed two small convolution kernels for improved resolution and fidelity: the spatially constrained Wiener filter and a parametric cubic convolution (designated 2D-5PCC-R). Subject to constraints, both have been optimized with respect to maximum end-to-end system fidelity. Experimental results for a simulated imaging system and for real images indicate the effectiveness of the small-kernel methods for increasing resolution and fidelity. Visually, the superresolution images from the small-kernel Wiener filter are slightly sharper than images from 2D-5PCC-R, but both small-kernel methods yield significant quantitative and qualitative improvements.

Additional work to develop efficient implementations of the small-kernel superresolution methods is required. Even with the efficiency of one-pass restoration and reconstruction by use of small kernels, superresolution requires significant processing. Each low-resolution image pixel in the kernel's region of support around each superresolution pixel contributes to the output value. Superresolution processing of K images, with kernel support of $[-S, S] \times [-S, S]$ pixels and a superresolution increase of $R \times R$, requires $4KS^2R^2$ floating-point multiplications and additions. If the distribution of low-resolution pixels varies with respect to the superresolution pixels, multiple kernels (each with KS^2 weights) should be used in the computation. These issues make implementation, especially in hardware, challenging.

Appendix A. Components of the 2D-5PCC-R Cubic Convolution Kernel for Superresolution. Restoration and Reconstruction [Eq. (21)]

$$f_0(x, y) = \begin{cases} x^2y^2 - x^2 - y^2 + 1 & 0 \le x \le 1, \quad 0 \le y \le 1, \\ (2xy^2 - 2x - 2y^2 + 2)(x - 2)^2 & 1 < x \le 2, \quad 0 \le y \le 1, \\ (4xy - 4y - 4x + 4)(x - 2)^2(y - 2)^2 & 1 < x \le 2, \quad 1 < y \le 2, \\ (2x^2y - 2y - 2x^2 + 2)(y - 2)^2 & 0 \le x \le 1, \quad 1 < y \le 2, \end{cases}$$

$$f_1(x, y) = \begin{cases} x^3y^3 - x^2y^2 & 0 \le x \le 1, \quad 0 \le y \le 1, \\ (5xy^3 - 4xy^2 - 4y^3 + 3y^2)(x - 2)^2 & 1 < x \le 2, \quad 0 \le y \le 1, \\ (9xy - 8y - 8x + 7)(x - 2)^2(y - 2)^2 & 1 < x \le 2, \quad 1 < y \le 2, \\ (5x^3y - 4x^2y - 4x^3 + 3x^2)(y - 2)^2 & 0 \le x \le 1, \quad 1 < y \le 2, \end{cases}$$

$$f_2(x, y) = \begin{cases} x^3y^2 - 2x^2y^2 + x^2y^3 & 0 \le x \le 1, \quad 0 \le y \le 1, \\ (4xy^3 - 3xy^2 - 3y^3 + 2y^2)(x - 2)^2 & 1 < x \le 2, \quad 0 \le y \le 1, \\ (8xy - 7y - 7x + 6)(x - 2)^2(y - 2)^2 & 1 < x \le 2, \quad 1 < y \le 2, \\ (4x^3y - 3x^2y - 3x^3 + 2x^2)(y - 2)^2 & 0 \le x \le 1, \quad 1 < y \le 2, \end{cases}$$

$$f_3(x, y) = \begin{cases} x^3 - x^2 - y^2 + y^3 & 0 \le x \le 1, \quad 0 \le y \le 1, \\ (2xy^3 - 2xy^2 + x + y^2 - y^3 - 1)(x - 2)^2 & 1 < x \le 2, \quad 0 \le y \le 1, \\ (4xy - 3x - 3y + 2)(x - 2)^2(y - 2)^2 & 1 < x \le 2, \quad 1 < y \le 2, \\ (2x^3y - 2x^2y + y + x^2 - x^3 - 1)(y - 2)^2 & 0 \le x \le 1, \quad 1 < y \le 2, \end{cases}$$

$$f_4(x, y) = \begin{cases} 5x^2 - 6x^2y^2 + 5y^2 - 4 & 0 \le x \le 1, \quad 0 \le y \le 1, \\ (13y^2 - 14xy^2 + 12x - 11)(x - 2)^2 & 1 < x \le 2, \quad 0 \le y \le 1, \\ (30x + 30y - 32xy - 28)(x - 2)^2(y - 2)^2 & 1 < x \le 2, \quad 1 < y \le 2, \\ (13x^2 - 14x^2y + 12y - 11)(y - 2)^2 & 0 \le x \le 1, \quad 1 < y \le 2, \end{cases}$$

$$f_5(x, y) = \begin{cases} 4x^2 - 3x^2y^2 + 4y^2 - 4 & 0 \le x \le 1, \quad 0 \le y \le 1, \\ (5y^2 - 4xy^2 + 8x - 8)(x - 2)^2 & 1 < x \le 2, \quad 0 \le y \le 1, \\ (4x + 4y - 7)(x - 2)^2(y - 2)^2 & 1 < x \le 2, \quad 1 < y \le 2, \\ (5x^2 - 4x^2y + 8y - 8)(y - 2)^2 & 0 \le x \le 1, \quad 1 < y \le 2. \end{cases}$$

References

1. M. G. Kang and S. Chaudhuri, "Super-resolution image reconstruction," IEEE Signal Process. Mag. **20**(3), 19–20 (2003).
2. E. Choi, J. Choi, and M. G. Kang, "Super-resolution approach to overcome physical limitations of imaging sensors: an overview," Int. J. Imag. Syst. Technol. **14,** 36–46 (2004).
3. S. C. Park, M. K. Park, and M. G. Kang, "Super-resolution image reconstruction: a technical overview," IEEE Signal Process. Mag. **20**(3), 21–36 (2003).
4. R. C. Hardie, K. J. Barnard, J. G. Bognar, E. E. Armstrong, and E. A. Watson, "High-resolution image reconstruction from a sequence of rotated and translated frames and its application to an infrared imaging system," Opt. Eng. **37,** 247–260 (1998).
5. M. Elad and A. Feuer, "Restoration of a single superresolution image from several blurred, noisy, and undersampled measured images," IEEE Trans. Image Process. **6,** 1646–1658 (1997).
6. C. L. L. Hendriks and L. J. V. Vliet, "Improving resolution to reduce aliasing in an undersampled image sequence," in *Sensors and Camera Systems for Scientific, Industrial, and Digital Photography Applications,* M. M. Blouke, N. Sampat, G. M. Williams, and T. Yeh, eds., Proc. SPIE **3965,** 1–9 (2000).
7. H. Foroosh, J. B. Zerubia, and B. Marc, "Extension of phase correlation to subpixel registration," IEEE Trans. Image Process. **11,** 188–200 (2002).
8. M. Irani and S. Peleg, "Improving resolution by image registration," CVGIP Graph. Models Image Process. **53,** 231–239 (1991).
9. M. S. Alam, J. G. Bognar, R. C. Hardie, and B. J. Yasuda, "Infrared image registration and high-resolution reconstruction using multiple translationally shifted aliased video frames," IEEE Trans. Instrum. Meas. **49,** 915–923 (2000).
10. T. M. Lehmann, C. Gonner, and K. Spitzer, "Survey: interpolation methods in medical image processing," IEEE Trans. Med. Imag. **18,** 1049–1075 (1999).
11. M. L. Stein, *Interpolation of Spatial Data: Some Theory for Kriging* (Springer-Verlag, 1999).
12. J. Ruiz-Alzola, C. Alberola-López, and C. F. Westin, "Adaptive kriging filters for multidimensional signal processing," Signal Process. **85,** 413–439 (2005).
13. A. K. Katsaggelos, *Digital Image Restoration* (Springer-Verlag, 1991).
14. R. L. Lagendijk and J. Biemond, "Basic methods for image restoration and identification," in *Handbook of Image and Video Processing,* A. Bovik, ed. (Academic, 2000).
15. M. K. Ng and N. K. Bose, "Mathematical analysis of superresolution methodology," IEEE Signal Process. Mag. **20,** 62–74 (2003).
16. R. Y. Tsai and T. S. Huang, "Multiframe image restoration and registration," in *Advances in Computer Vision and Image Processing*, T. S. Huang, ed. (JAI Press 1984), pp. 317–339.
17. S. P. Kim, N. K. Bose, and H. M. Valenzuela, "Recursive reconstruction of high resolution image from noisy undersampled multiframes," IEEE Trans. Acoust. Speech Signal Process. **38,** 1013–1027 (1990).
18. S. P. Kim and W.-Y. Su, "Recursive high-resolution reconstruction of blurred multiframe images," IEEE Trans. Image Process. **2,** 534–539 (1993).
19. R. R. Schultz and R. L. Stevenson, "Extraction of high-resolution frames from video sequences," IEEE Trans. Image Process. **5,** 996–1011 (1996).
20. M. Elad and Y. Hel-Or, "A fast super-resolution reconstruction algorithm for pure translational motion and common space-invariant blur," IEEE Trans. Image Process. **10,** 1187–1193 (2001).
21. N. Nguyen and P. Milanfar, "A computationally efficient super-resolution image reconstruction algorithm," IEEE Trans. Image Process. **10,** 573–583 (2001).
22. S. Farsiu, D. Robinson, M. Elad, and P. Milanfar, "Advances and challenges in superresolution," Int. J. Imag. Syst. Technol. **14,** 47–57 (2004).
23. S. Farsiu, D. Robinson, M. Elad, and P. Milanfar, "Fast and robust multiframe super resolution," IEEE Trans. Image Process. **13,** 1327–1344 (2004).
24. C. L. Fales, F. O. Huck, J. A. McCormick, and S. K. Park, "Wiener restoration of sampled image data: end-to-end analysis," J. Opt. Soc. Am. A **5,** 300–314 (1988).
25. E. H. Linfoot, "Transmission factors and optical design," J. Opt. Soc. Am. **46,** 740–752 (1956).
26. S. E. Reichenbach and S. K. Park, "Small convolution kernels for high-fidelity image restoration," IEEE Trans. Signal Process. **39,** 2263–2274 (1991).
27. R. G. Keys, "Cubic convolution interpolation for digital image processing," IEEE Trans. Acoust. Speech Signal Process. **29,** 1153–1160 (1981).
28. S. K. Park and R. A. Schowengerdt, "Image reconstruction by parametric cubic convolution," Comput. Vision Graph. Image Process. **23,** 258–272 (1983).
29. S. E. Reichenbach and J. Shi, "Two-dimensional cubic convolution for one-pass image restoration and reconstruction," in *International Geoscience and Remote Sensing Symposium* (Institute of Electrical and Electronics Engineers, 2004), pp. 2074–2076.
30. J. Shi and S. E. Reichenbach, "Image image interpolation by two-dimensional parametric cubic convolution," IEEE Trans. Image Process. (to be published).
31. P. Milanfar, Resolution enhancement software, www.soe.ucsc.edu/~milanfar/SR-software.htm (2004).
32. Nebraska Department of Natural Resources, Digital Orthophoto Quadrangle Database, www.dnr.state.ne.us/databank/coq.html (2004).
33. T. Blu, P. Thévenaz, and M. Unser, "MOMS: maximal-order interpolation of minimal support," IEEE Trans. Image Process. **10,** 1069–1080 (2001).
34. R. A. Schowengerdt, *Remote Sensing: Models and Methods for Image Processing*, 2nd ed. (Academic, 1997).
35. K. R. Castleman, *Digital Image Processing* (Prentice-Hall, 1979).
36. S. E. Reichenbach, S. K. Park, and R. Narayanswamy, "Characterizing digital image acquisition devices," Opt. Eng. **30,** 170–177 (1991).